Physica B 715 (2025) 417566

Contents lists available at ScienceDirect

Physica B: Condensed Matter

journal homepage: www.elsevier.com/locate/physb

A comparative study on the optoelectronic properties of sputtered $BiFeO_3$ and $BiMnO_3$ thin films as solar absorbers

Rayene Merah [a], Warda Darenfad [a,*], Kamel Mirouh [a], Noubeil Guermat [b,c], Nadir Bouarissa [d,**]

[a] Thin Films and Interfaces Laboratory (LCMI), University of Constantine 1, 25000, Constantine, Algeria
[b] Department of Electronics, Faculty of Technology, University of M'sila, PO Box 166 Ichebilia, 28000, M'sila, Algeria
[c] Laboratory of Electronic Materials Studies for Medical Applications (LEMEAMED), University of Constantine 1, 25000, Constantine, Algeria
[d] Laboratory of Materials Physics and Its Applications, University of M'sila, 28000, M'sila, Algeria

ARTICLE INFO

Keywords:
Thin films
$BiFeO_3$
$BiMnO_3$
Spray pyrolysis
Hydrophobic
Heterojunctions

ABSTRACT

In this study, the ferroelectric materials $BiFeO_3$ (BFO) and $BiMnO_3$ (BMO) were successfully synthesized on standard glass substrates using a cost-effective spray pyrolysis method, and their optoelectronic properties were comprehensively compared for the first time. X-ray diffraction analysis revealed that BFO exhibits a rhombohedral crystal structure, while BMO adopts a monoclinic structure. Raman spectroscopy provided further confirmation of the distinct crystal structures of these films. EDS analysis confirms the presence of selective elements in the synthesized samples. Atomic force microscopy (AFM) analysis demonstrated the significant impact of these ferroelectric materials on the surface morphology. The BFO film exhibited a significantly higher surface roughness at 512.1 nm than BMO at 29.38 nm. Contact angle analysis revealed that both samples were hydrophobic, with BFO and BMO exhibiting angles of 100° and 93° respectively. UV–visible transmission spectra indicated that the BMO film had a low light transmittance at 2 % and a smaller optical band gap of 1.2 eV. Electrical characterization showed that the BMO film had the lowest electrical resistivity ($\rho = 1.90 \times 10^{+1}$ Ω cm) with a carrier density of $-2.193 \times 10^{+14}$ (n-type conductivity), compared to BFO with $\rho = 8.344 \times 10^{+4}$ Ω cm and a carrier density of $9.895 \times 10^{+11}$ cm^{-3} (p-type conductivity). The current-voltage (I-V) characteristics recorded for FTO/BFO/Au and FTO/NiO/BMO/Au cells showed rectifying behavior with ideality factors ranging from 2.67 to 1.38 and series resistances from $3.81 \times 10^{+3}$ Ω–13.32 Ω, and high contact barriers from 0.70 eV to 0.52 eV, respectively. The reduction in ideality factor and series resistance suggests that the sputter-deposited BMO improves the behavior of thin-film solar cells toward near-ideal behavior by passivating the interface states.

1. Introduction

Inorganic thin-film photovoltaic technologies have traditionally relied on materials such as CdTe [1], a-Si:H [2], a-Si:H [2], $CuInSe_2$ [3], $CuInGeSe_4$ [4], $SnSb_2S_4$ [5], and GaP [6], which provide high efficiency and long-term stability. Their widespread industrial use is mainly due to the maturity of fabrication processes and their proven reliability. More recently, hybrid perovskite solar cells have revolutionized the field, achieving power conversion efficiencies above 20 % [2]. However, these materials still face significant challenges related to environmental and structural stability. In this context, attention has shifted to inorganic oxide perovskites [7], which are characterized by their environmental safety, chemical stability, natural abundance, and compatibility with low-temperature synthesis processes thus contributing to cost reduction. Among these, multiferroic perovskites [8] are particularly promising due to their spontaneous electric polarization below the Curie temperature, which is reversible under an electric field. This property facilitates efficient charge separation in photovoltaic devices. Previous research has mainly focused on classical ferroelectric oxides such as $LiNbO_3$ [9], $BaTiO_3$ [10], and $Pb(Zr,Ti)O_3$ [11]. However, their wide band gaps (ranging from 3 to 5 eV) limit their photovoltaic efficiency, primarily due to the strong electronegativity difference between transition metal cations and oxygen, which broadens the band gap [12]. Conversely, bismuth-based perovskites such as $BiFeO_3$ (BFO) and $BiMnO_3$ (BMO) have emerged as promising alternatives. The Bi^{+3} ion, with its $6s^2$ lone pair electrons, helps stabilize ferroelectric distortion similarly to Pb^{+2},

---

* Corresponding author.
** Corresponding author.
E-mail addresses: daranfed.warda@umc.edu.dz (W. Darenfad), n_bouarissa@yahoo.fr (N. Bouarissa).

https://doi.org/10.1016/j.physb.2025.417566
Received 21 April 2025; Received in revised form 2 July 2025; Accepted 3 July 2025

while offering a lead-free, environmentally friendly option suitable for photovoltaic applications [12]. This study aims to replace conventional ferroelectric oxides with BFO and BMO in order to overcome the limitations associated with wide band gaps and to optimize photovoltaic performance. These materials have recently been the subject of numerous applications, including lithium-ion batteries [13,14], photocatalysis [15,16], sensors [17,18], and solar devices. BFO is characterized by its low production cost [19], a moderate band gap (~2.67 eV), and strong spontaneous polarization [12]. Its stable ferroelectric and magnetic properties at room temperature, combined with good charge carrier mobility and a high optical absorption coefficient, make it a promising material for solar energy conversion [20]. For instance, Li et al. [21] demonstrated that BFO thin films can serve as efficient absorber layers in TiO_2/BFO heterojunctions, achieving a solar conversion efficiency of 0.1177 %. Similarly, Sui et al. [22] reported a higher efficiency of 3.67 % for a thin-film heterostructure based on FTO/TiO_2/BFO. Meanwhile, BMO also shows strong potential as an absorber layer in photovoltaic devices. Its narrow band gap (~1.25 eV) facilitates photon absorption over a broad range of the solar spectrum, particularly in the visible region [23]. Its ferroelectric nature promotes efficient charge separation, and its lead-free composition offers an environmentally friendly alternative to traditional lead-based perovskites. These combined properties position BMO as a promising candidate for next-generation photovoltaic technologies. As an example, Chakrabartty et al. [23] reported a conversion efficiency of 4.2 % for a Nb:STO/BMO heterojunction. Although BFO and BMO exhibit remarkable properties, their integration into photovoltaic devices remains limited by several challenges. These include high leakage currents, the formation of secondary phases after synthesis, and occasionally imperfect crystallinity. The deposition method plays a critical role in controlling these parameters, directly affecting phase purity, crystallite size, and the structural quality of thin films. Among the various deposition techniques, spray pyrolysis stands out for its simplicity, low cost, and ability to produce films over large areas at moderate temperatures using diverse precursors. However, this method has certain limitations, such as thickness inhomogeneity, surface roughness, poor adhesion, and non-uniform spraying. These constraints can be effectively addressed through careful optimization of deposition parameters, including pressure, spray rate, and substrate temperature.

To date, to the best of our knowledge, no comparative study has been reported on BFO and BMO thin films deposited on standard glass substrates using spray pyrolysis. This study therefore aims to fill this gap by conducting an in-depth comparative analysis of the structural, optical, electrical, and wettability properties of these materials. While BFO has been extensively studied, available data on the optoelectronic and wettability characteristics of BMO films remain limited. Furthermore, to our knowledge, no study has yet reported the electrical performance of a FTO/NiO/BMO/Au heterojunction. The objective of this work is therefore to optimize the physicochemical properties of BFO and BMO films prepared by spray pyrolysis, in order to assess their potential as low-band-gap ferroelectric absorber layers for high-efficiency thin-film solar cells.

2. Experimental procedure

In this study, $BiFeO_3$ and $BiMnO_3$ thin films were elaborated on standard glass substrates using spray pyrolysis technique the Holmarc type (see Fig. 1). For the synthesis of the $BiFeO_3$ thin film, solutions were prepared by dissolving equimolar concentrations (0.1 M) of bismuth nitrate pentahydrate ($Bi(NO_3)_3.5H_2O$) and ferric nitrate nonahydrate ($Fe(NO_3)_3.9H_2O$) separately in 10 mL of deionized water. Each solution was subjected to continuous stirring at room temperature for 1 h to ensure full dissolution and uniformity. After this initial mixing, 3 mL of diluted nitric acid (HNO_3) was carefully added dropwise to the bismuth nitrate solution. This solution was then stirred for an additional 15 min to allow thorough interaction of the reagents and to stabilize the solution for deposition. Similarly, for the $BiMnO_3$ thin film, 0.1 M equimolar concentration of bismuth nitrate pentahydrate ($Bi(NO_3)_3.5H_2O$) and manganese (II) acetate tetrahydrate ($C_4H_6MnO_4.4H_2O$) was used. Each precursor compound was independently dissolved in 10 mL of deionized

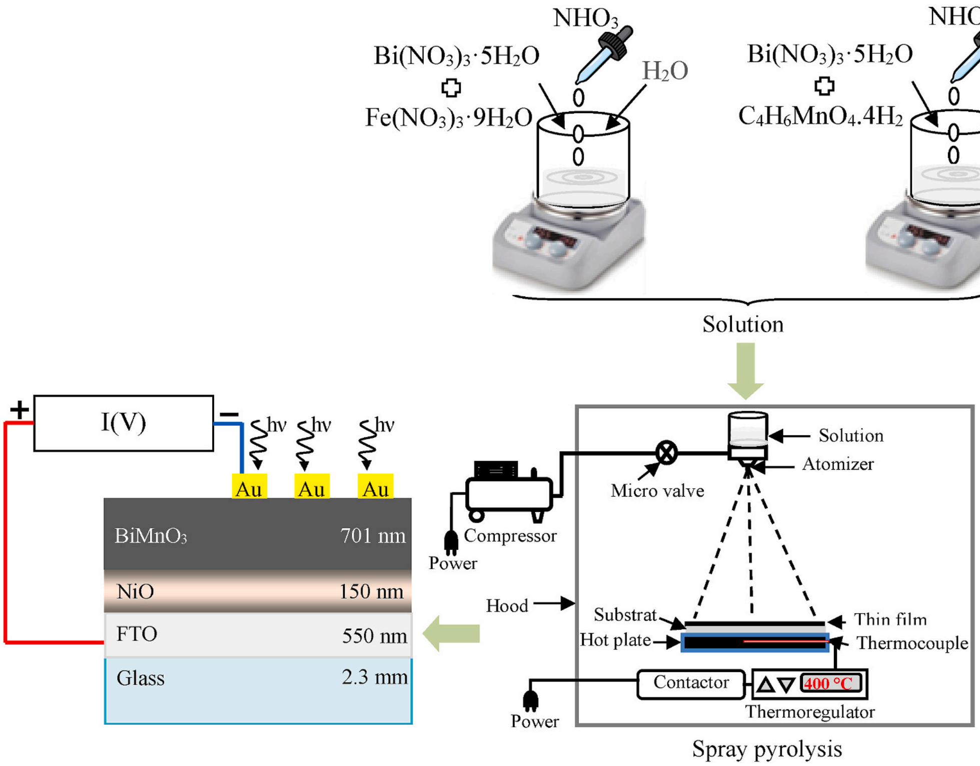

Fig. 1. Schematic diagram of the Holmarc-type spray technique.

water, with continuous stirring at room temperature for 1 h. As with the BFO preparation, 3 mL of HNO_3 was added dropwise to the bismuth nitrate base solution, followed by 15 min of additional stirring. For both $BiFeO_3$ and $BiMnO_3$ thin films, the substrate was maintained at a constant temperature of 400 °C. The precursor solution was sprayed at a controlled flow rate of 500 μL/min, and the nozzle-to-substrate distance was precisely set at 15 cm. Compressed air was used at a fixed pressure of 1 mbar. After the deposition process, the thin films were post-annealed at 500 °C for 1 h in an ambient atmosphere. The NiO/$BiMnO_3$ heterojunction was created using a $BiMnO_3$ thin film as the base layer. The NiO layer was also prepared through spray pyrolysis using the same deposition system. The spray solution consisted of 0.1 M dehydrated nickel acetate dissolved in distilled water, with the substrate temperature set at 350 °C and a flow rate of 500 μL/min. The resulting NiO film had a thickness of 150 nm. Additionally, a thin layer of $BiFeO_3$ was combined with FTO to develop p-n device architecture. To complete the final devices, a gold layer was deposited as the back contact, forming the configurations Au/$BiMnO_3$/NiO/FTO and Au/$BiFeO_3$/FTO, as shown in Fig. 2.

The structural properties of the films were characterized using X-ray diffraction (XRD) with a Philips X'Pert system, employing Cu Kα radiation ($\lambda = 0.154056$ nm). Diffraction data were collected at room temperature, with 2θ values ranging from 20° to 80°. Raman spectroscopy at room temperature using a HORIBA LabRAM with a 633 nm laser was used to probe the vibrational modes of the film. The EDS spectra were acquired using a Thermo Fisher Apreo 2C scanning electron microscope (SEM), equipped with a field emission gun (FEG-Schottky) electron source and an ultra-high-resolution Gemini column. Surface topography was analyzed point by point using contact-mode AFM with a Nanosurf Flex-Axiom C3000 over a 5 μm × 5 μm area, producing detailed 2D and 3D images. For additional surface characterization, static contact angle measurements were performed under ambient conditions using a system fabricated in our laboratory, 5 μL distilled water droplet was deposited, and measurements were taken 5 s later. Optical transmission in the UV–visible range (300–1000 nm) was measured using a Shimadzu UV-3101 PC spectrophotometer. Film thickness was measured with a MicroXam-100 optical profilometer using white light interferometry across a step edge between coated and uncoated areas. The electrical properties of the films resistivity, carrier concentration, and mobility were measured at room temperature using the Van der Pauw method with an Ecopia HMS-3000 Hall effect system. The current–voltage (I–V) characteristics of the heterojunction were investigated using a high-resolution spectral photoacoustic spectrometer, fabricated at the LCCNS laboratory of Setif 1 University. During the measurement, a variable bias voltage from 0 V up to a value close to the open-circuit voltage (V_{oc}) was applied across the two electrodes of the photovoltaic device. The photocurrent generated under continuous illumination was recorded at each voltage increment.

3. Results and discussion

3.1. Structural properties

The structural properties of the BFO and BMO thin films were analyzed using XRD, and the corresponding patterns are shown in Fig. 3. As illustrated in Fig. 3(a), BFO film exhibits a polycrystalline structure characterized by sharp and well-defined peaks corresponding to the (012), (104), (110), (202), (204), (116), (018), and (128) crystal planes.

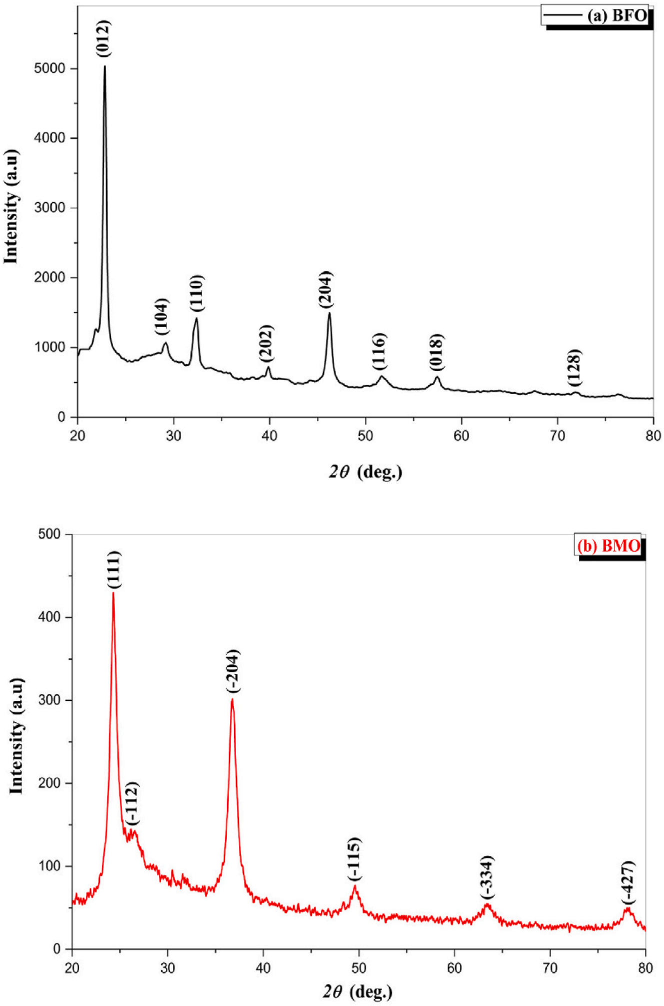

Fig. 3. XRD spectra of thin films of BFO and BMO.

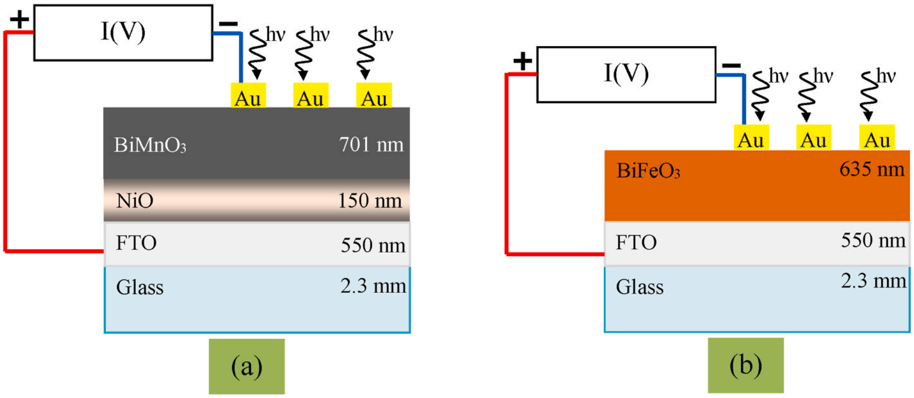

Fig. 2. Diagram of the devices: (a) Glass/FTO/NiO/$BiMnO_3$/Au and (b) Glass/FTO/$BiFeO_3$/Au.

These reflections are indexed to the rhombohedral phase of BFO with space group *R*3*c*, in accordance with JCPDS card No. 86–1518 [17,24]. The absence of secondary peaks confirms the formation of a single-phase film, free from impurity phases such as Bi_2O_3 or Fe_2O_3. Moreover, the pronounced intensity of the (012) diffraction peak suggests a preferential orientation along this plane, indicating that the crystallites exhibit oriented growth. These findings are in good agreement with previously reported results in the literature [17].

Fig. 3(b) shows the XRD pattern of the BMO film prepared by spray pyrolysis. According to Singh et al. [25], obtaining a pure phase of BMO is challenging due to the frequent presence of secondary phases. The diffraction peaks observed at 2θ angles of 24.15°, 26.75°, 36.79°, 49.45°, 63.47°, and 78.19° correspond to the (111), (−112), (−204), (−115), (−334) and (−427) crystal planes, respectively, confirming the formation of a monoclinic crystal structure [25]. Moreover, the peak at $2\theta = 26.75°$ indicates the presence of Bi_2O_3 as a secondary phase impurity. Similar results have been reported by Umoh et al. [26], Meng et al. [27], and Ibrahim et al. [28].

The crystallite size (D), lattice strain (ε) and dislocation density (δ) were estimated using the equations [29–31]:

$$D = \frac{0.9\lambda}{\beta \cos\theta} \tag{1}$$

$$\varepsilon = \frac{\beta}{4 \tan\theta} \tag{2}$$

$$\delta = \frac{1}{D^2} \tag{3}$$

These calculations were based on the values of β (full width at half maximum in radian), λ (wavelength of CuK radiation, 0.15406 nm), θ (angle of diffraction wavelength). Table 1 provides a summary of the calculated structural parameters.

The crystallographic analysis revealed that the D was 30.8 nm for the BFO film and 13.1 nm for the BMO film, confirming their nanostructured nature. Notably, the BFO film exhibited a significantly larger D than BMO. This discrepancy can be attributed to the higher density of structural defects typically observed in BMO thin films. These defects such as dislocations (as reported in Table 1), stacking faults, and lattice distortions introduce internal strain and disrupt long-range crystallographic order, thereby hindering crystal growth. The origin of these structural imperfections is likely related to the complex interactions occurring within the MnO_6 octahedra of the BMO lattice, which promote grain fragmentation and ultimately limit crystallite development.

Using Raman spectrometer, we examined the structure of BFO and BMO thin films deposited at substrate temperature of 400 °C by spray pyrolysis. All tests were performed with a 633 nm laser source at room temperature. The spectra obtained are presented in Fig. 4 above. The Raman spectrum of the BFO sample is shown in Fig. 4(a). According to group theory analysis, the BFO is expected to exhibit 13 active Raman vibration modes, namely $4A_1 + 9E$ [24,32]. The A_1 modes are polarized in the z direction, while the doubly degenerate E modes are polarized in the x-y plane. Among the 13 vibrational modes at the center of the BFO region, Bi atoms contribute only in lower wavenumber modes up to 167 cm^{-1}, while modes above 262 cm^{-1} are dominated by oxygen atoms. Fe atoms participate in vibrational modes between 152 and 262 cm^{-1}. The optical modes of A_1 and E are identified in Fig. 4(a), where the peaks at 70.01, 131.01, 166.23, 220.03, 262.88, 349.65, 475.08 and 622.85 cm^{-1} correspond to E_{-1}, $A_{1\text{-}1}$, $A_{1\text{-}2}$, $A_{1\text{-}3}$, E_{-3}, E_{-5}, E_{-7} and E_{-9} respectively. These values are in agreement with the results calculated by first principle based on density functional theory [33] thus confirming the rhombohedral R_{3c} structure of the BFO film. The Raman spectrum of BMO, recorded at room temperature, is illustrated in Fig. 4(b). Peak positions at 76.05, 177.14, 313.40, and 586.08 cm^{-1} correspond to distinct Raman modes: Bi, (R_Y, R_Xz ((Bg)), δ(MnO_6), and $\upsilon_3 + \upsilon_6$, respectively, as noted in Ref. [34]. According to our assignment, low-frequency modes (below 100 cm^{-1}) are attributed to the oscillations of the Bi atom, represented by B_{ix}, B_{iY}, and B_{iz} modes. Modes related to the coordinated rotations of the MnO_6 octahedron (R_X, R_Y, and Rz) appear between 165 and 200 cm^{-1}. Mid-frequency modes, ranging from 240 to 400 cm^{-1}, involve a mix of octahedral rotations and bending deformations, δ(MnO_6). Finally, bending and stretching modes (Fig. 4(b)) are observed at frequencies above 500 cm^{-1}. The experimental Raman peaks identified are attributed to the monoclinic structure, consistent with findings in Refs. [34,35].

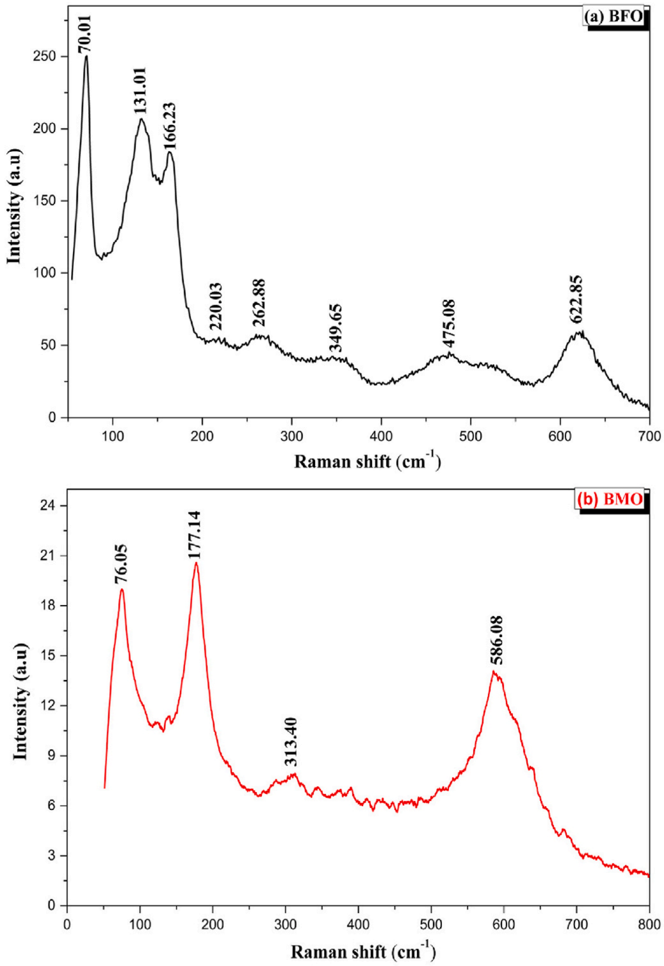

Fig. 4. Raman Spectra of BFO and BMO thin films.

The Raman spectrum of BFO is characterized by sharp, well-defined, and intense peaks, indicating high crystallinity, low defect density, and an ordered crystal structure. Such features are typical of a well-formed and weakly strained phase. Moreover, the pronounced peak intensity reflects the good structural quality of the thin films. In comparison, the Raman spectrum of the BMO film exhibits broader, less resolved, and weaker bands, suggesting lower crystallinity. This behavior may be attributed to a more disordered structure, a higher defect density, or the presence of lattice distortions. Notably, these distortions can play a beneficial role by enhancing certain optical and electrical properties of the BMO film. The Raman observations align with the XRD results,

Table 1
Structural parameters of BFO and BMO films.

Samples	Peak	Crystallite size, D (nm)	Strain, ε ($\times 10^{-3}$)	Dislocation density, δ ($\times 10^{-3}$ nm^{-2})	Thickness, (nm)
BFO	(012)	30.8	3.13	1.054	635
BMO	(111)	13.1	4.78	5.827	701

confirming the difference in crystalline quality between the two films.

3.2. Compositional analysis (EDS) and surface properties (AFM and contact angle)

Fig. 5 shows the EDX spectra of BFO and BMO thin films. The analyses confirm the presence of the main constituent elements in both compounds. For BFO, the measured atomic percentages are 16.3 % for Bi, 18.2 % for Fe, and 65.5 % for O. This composition is generally close to the ideal stoichiometry of Bi:Fe:O = 1:1:3, although a slight bismuth deficiency is observed, likely due to partial loss during the deposition process. For BMO, the atomic percentages are 21.6 % for Bi, 18.6 % for Mn, and 59.8 % for O, which closely matches the expected chemical formula. This atomic distribution indicates good chemical homogeneity and efficient incorporation of the elements into the film matrix. Overall, both films exhibit a composition near their nominal stoichiometry, with BMO showing slightly better chemical balance.

Fig. 6 presents atomic force microscopy (AFM) images and static water contact angle (CA) measurements for BFO and BMO thin films. The measured CA for water droplets on the BFO and BMO surfaces were 100° and 93°, respectively, as listed in Table 2. These values confirm the hydrophobic nature of both films (CA $> 90°$, [36–38]). Similar hydrophobic behavior was reported by Darenfad et al. [39] and Nezzari et al. [40] for CuO and Co_3O_4 absorber films elaborated by spray pyrolysis. This hydrophobicity is attributed to the effect of surface roughness and the spray pyrolysis technique used [40]. According to Bellili et al. [41], such surface behavior can be explained by the Cassie-Baxter model, which suggests that air pockets trapped between the water droplet and the textured surface enhance the contact angle. In the context of solar cell applications, hydrophobic surfaces offer several advantages: (i) they enhance device durability and performance in humid environments, (ii) minimize corrosion under adverse atmospheric conditions [37,38], (iii) reduce water and contaminant accumulation, thereby improving light absorption and overall energy conversion efficiency [42], and (iv) simplify cleaning and maintenance, which can prolong the operational lifetime of photovoltaic components [39,42]. The CA measurements align well with the AFM results presented in Fig. 6. Specifically, the BFO film demonstrates a considerably higher root-mean-square (RMS) surface roughness of 512.1 nm compared to 29.38 nm for the BMO film, indicating a more textured surface. Correspondingly, the BMO film exhibits a slightly lower CA (93°) than the BFO film (CA = 100°) which suggests a less rough. This reduced surface roughness in BMO films is advantageous for optoelectronic applications, as it helps suppress unwanted light scattering and surface reflection, thereby enhancing light absorption within the active layer. Moreover, the improved wettability associated with the smoother BMO surface facilitates stronger interfacial adhesion between the absorber layer and adjacent functional layers in thin-film solar cells. Such enhanced adhesion contributes to the formation of a more stable and continuous interface, which can suppress interfacial defects and charge carrier recombination. Consequently, this contributes to improved charge transport and increased photovoltaic efficiency of the device.

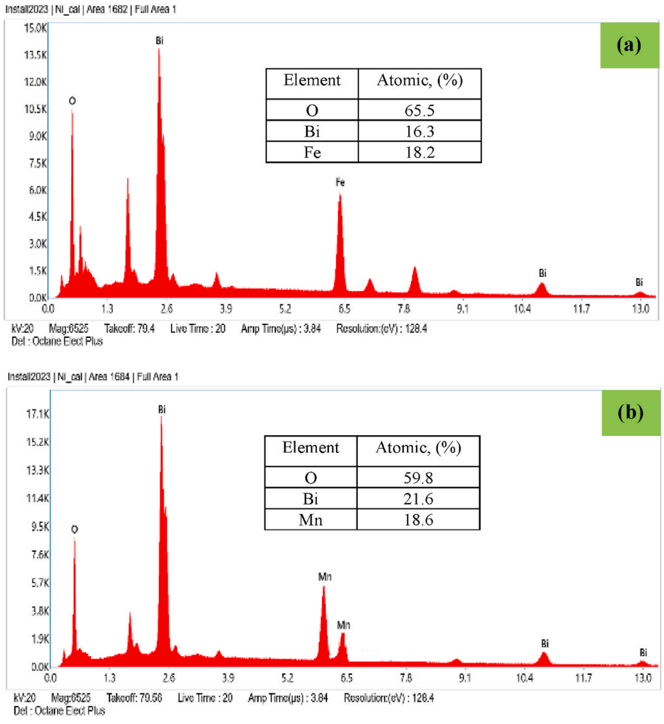

Element	Atomic, (%)
O	65.5
Bi	16.3
Fe	18.2

Element	Atomic, (%)
O	59.8
Bi	21.6
Mn	18.6

Fig. 5. EDS spectra of: a) BFO and b) BMO thin films.

3.3. Optical properties

The optical transmittance spectra of BFO and BMO thin films are shown in Fig. 7, illustrating their light transmission behavior within the visible range (400–800 nm). The BFO film exhibits a moderate average transmittance of approximately 17 %, whereas the BMO film displays a significantly lower transmittance of around 2 % across the same spectral range. The higher transmittance observed in the BFO layer is likely due to its lower thickness (see Table 2) and its highly ordered and periodic crystal structure, which minimizes light scattering and absorption. In contrast, the markedly low transmittance of the BMO film suggests strong absorption of visible light, which can be attributed to an increased rate of electronic transitions between the valence and conduction bands. For wavelengths above 700 nm, a noticeable rise in transmittance is observed for BMO, indicating a possible shift in its optical absorption behavior. This enhanced absorption in the visible region may be related to structural defects and reduced D, as supported by the XRD analysis presented in Table 2. Such defects likely introduce localized electronic states within the band gap, thereby increasing subgap absorption. Moreover, the reduced transmittance in BMO could also stem from phonon-related interactions associated with the MnO_6 octahedra in its crystal lattice. These vibrational modes may further facilitate internal optical absorption, even in films with relatively low surface roughness. Compared to BFO, the significantly higher light absorption exhibited by BMO highlights its potential as an efficient absorber layer for photovoltaic applications. Its optical characteristics suggest that BMO can enhance solar cell performance by maximizing light harvesting and minimizing optical losses.

The optical band gap (Eg) is a key factor in determining the absorption threshold of thin films. In this study, we calculated the Eg values of BFO and BMO films using the Tauc model [43,44], which correlates with transmittance spectra. According to this method, Eg can be determined by plotting $(\alpha h\nu)^2$ as a function of $h\nu$ and then extrapolating the linear portion of the curve to intersect the energy axis where absorption is zero ($(\alpha h\nu)^2 = 0$), as shown in Fig. 8. Based on the analysis, the optical band gap was found to be 2.04 eV for BFO and 1.20 eV for BMO. However, conventional ferroelectric materials typically exhibit wide band gaps exceeding 3 eV [45], which significantly limits their ability to absorb visible light. Even BFO, with a relatively narrow Eg of 2.04 eV, can only absorb photons with wavelengths shorter than 460 nm representing roughly 20 % of the solar spectrum [46]. This inherently constrains the photovoltaic performance and limits the power conversion efficiency of ferroelectric-based solar cells [46]. In contrast, the lower band gap of 1.20 eV observed for BMO in this study indicates a significant enhancement in its light-harvesting capability, as evidenced by its improved optical absorption shown in Fig. 7. This narrower Eg allows the material to absorb a broader range of the solar spectrum, making it a more promising candidate for photovoltaic applications. Furthermore, the obtained Eg value is lower than the 1.3 eV reported by Shin et al. [47] for BMO films grown via epitaxial deposition. This

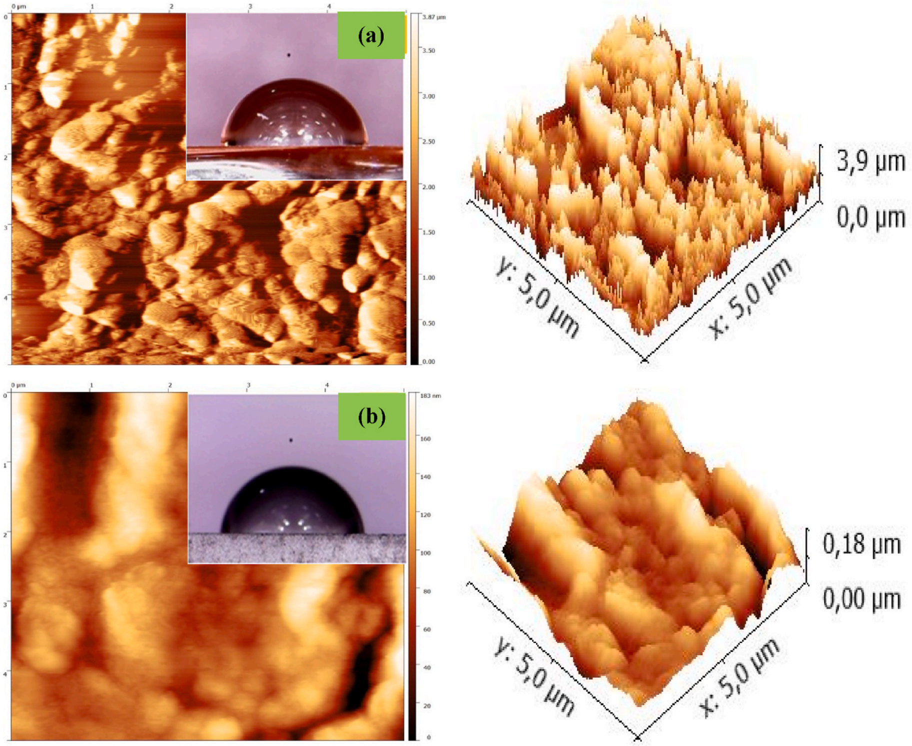

Fig. 6. AFM and contact angle images for (a) BFO and (b) BMO.

Table 2
Measured values of the contact angle and RMS of our films.

Samples	CA, (°)	RMS, (nm)
BFO	100	512.1
BMO	93	29.38

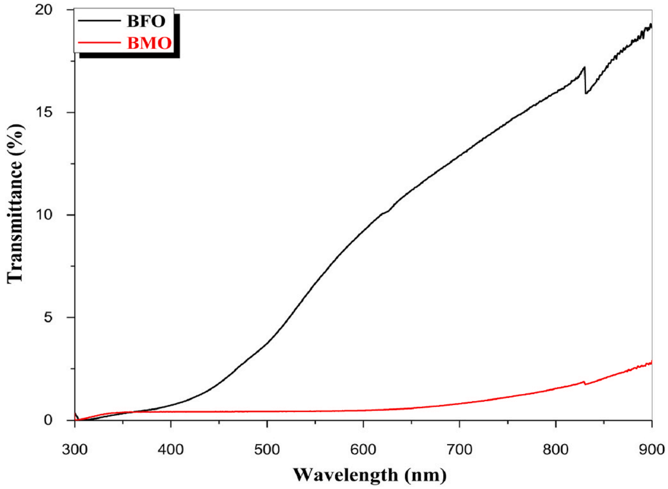

Fig. 7. Transmission spectra for BFO and BMO thin films.

difference is likely due to the use of the spray pyrolysis technique in our work, which may introduce structural or defect-related modifications that influence the electronic band structure. This observed reduction in band gap indicates a red shift in the absorption edge, suggesting enhanced light absorption in the lower-energy region of the spectrum. Such a shift is typically associated with the presence of localized defect states within the band structure, which are often introduced during the film growth process. Defects like vacancies, interstitials, and dislocations often act as trapping centers, which can lead to the formation of localized energy states near the band edges and reduce the optical band gap. These findings suggest that BMO, with its narrow bandgap, could be particularly valuable in designing high-absorption, low-band gap films for optoelectronic devices, enhancing the photovoltaic effect in thin-film solar cells. This comparative analysis supports the potential of BMO as an absorber layer, advancing the efficiency of thin-film solar cell technologies through improved light absorption and minimal optical loss.

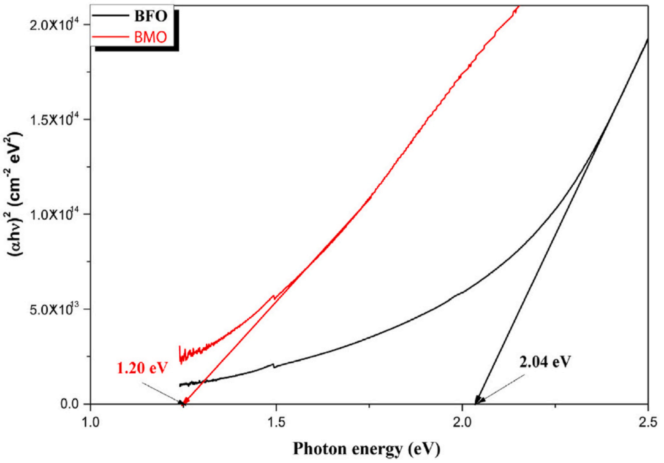

Fig. 8. The Variation of $(\alpha h\nu)^2$ as a function of $h\nu$ for Thin films of BFO and BMO.

3.4. *Electrical properties*

The electrical resistivity (ρ), Hall mobility (μ), and carrier concentration (n) of the various thin films were measured at room temperature using a Hall effect measurement system, and the results are presented in Table 3. The BFO film exhibits p-type conductivity, likely due to metal vacancies (Bi and Fe) within the film, which are thought to create acceptor levels and therefore yield p-type conductivity [48]. Conversely, the BMO thin film shows n-type conductivity [49]. The electrical resistivity of $BiMnO_3$ is approximately $1.90 \times 10^{+1}$ Ω cm, significantly lower than that of $BiFeO_3$, which is measured at $8.344 \times 10^{+4}$ Ω cm. This resistivity value for $BiFeO_3$ represents an improvement over that obtained by Mohamed et al. [50], who reported $2.85 \times 10^{+6}$ Ω cm for $BiFeO_3$ thin films elaborated by sol-gel. Additionally, the resistivity of BMO prepared by spray pyrolysis in our study ($\rho = 1.90 \times 10^{+1}$ Ω cm) also shows an improvement compared to the value of $1.85 \times 10^{+2}$ Ω cm obtained from films deposited using radiofrequency magnetron sputtering, as observed in the work by Umoh et al. [26]. Moreover, the particularly high resistivity of BFO is primarily attributed to its low free charge carrier density, which significantly limits its electrical conductivity. This phenomenon is further exacerbated by a high concentration of oxygen vacancies within the crystal lattice. These point defects act as trap centers for charge carriers by capturing electrons or holes, thereby hindering their mobility and leading to a notable increase in the overall resistivity of the material [51]. In contrast, BMO exhibits a much lower resistivity, which can be explained by a fundamentally different conduction mechanism. In the case of BMO, electrical transport is primarily governed by a small polaron hopping mechanism, involving mixed-valence manganese ions Mn^{+3} and Mn^{+4}. This configuration enables electrons to move in a thermally activated manner from Mn^{+3} to neighboring Mn^{+4} sites, thus facilitating charge transfer throughout the material [52]. Additionally, the low resistivity observed in BMO thin films correlates with their high charge carrier concentration (see Table 3), further supporting this finding. The reduced resistivity of BMO compared to BFO can also be linked to crystallite densification, which improves grain-to-grain connectivity and promotes more efficient charge transport. According to Hanif et al. [53], the low resistivity observed in BMO film is likely attributed to strain effects arising from the lattice mismatch between the substrate and the thin film. This behavior is in good agreement with the XRD analysis result presented in Table 1. Furthermore, the hydrophobic character of absorber layers has been found to positively influence their electrical performance in photovoltaic applications [39,40]. Prior studies by Darenfad et al. [39] and Nezzari et al. [40] demonstrated that hydrophobic thin films such as CuO and Co_3O_4, prepared via spray pyrolysis, exhibit low electrical resistivity. By comparison, the BMO-based layer displays low resistivity, which can be attributed to its surface less rough (RMS = 226.8 nm) and moderately hydrophobic character (CA = 93°). In contrast, the BFO film exhibits significantly higher resistivity, likely due to its highly hydrophobic surface (CA = 100°) and much greater surface roughness (RMS = 512.1 nm), as summarized in Table 2. These results emphasize the critical role of surface hydrophobicity and morphology in determining the electrical behavior of absorber layers. It can be concluded that a moderately hydrophobic surface (CA ≤ 93°, less rough) is favorable for enhancing both the electrical and optical properties of absorber films elaborated by spray pyrolysis in thin-film photovoltaic devices.

3.5. Analysis of the fabricated heterojunctions

Fig. 9(a and b) presents the current–voltage (I–V) characteristics of the BFO/FTO and BMO/NiO/FTO heterojunctions after thermal annealing at 300 °C for 1 h. The I–V analysis provides key insights into the diode junction parameters, including the series resistance (R_s), ideality factor (n), and saturation current (I_s). These parameters can be extracted using the following equation [6]:

Table 3
Electrical measurements of thin films of BFO and BMO.

Samples	Resistivity (ρ), (Ω. cm)	Mobility (μ), (cm^2/vs)	Carrier concentration (n), (cm^{-3})
BFO	$8.344 \times 10^{+4}$	7.561	$9.895 \times 10^{+11}$
BMO	$1.90 \times 10^{+1}$	$1.49 \times 10^{+1}$	$-2.193 \times 10^{+14}$

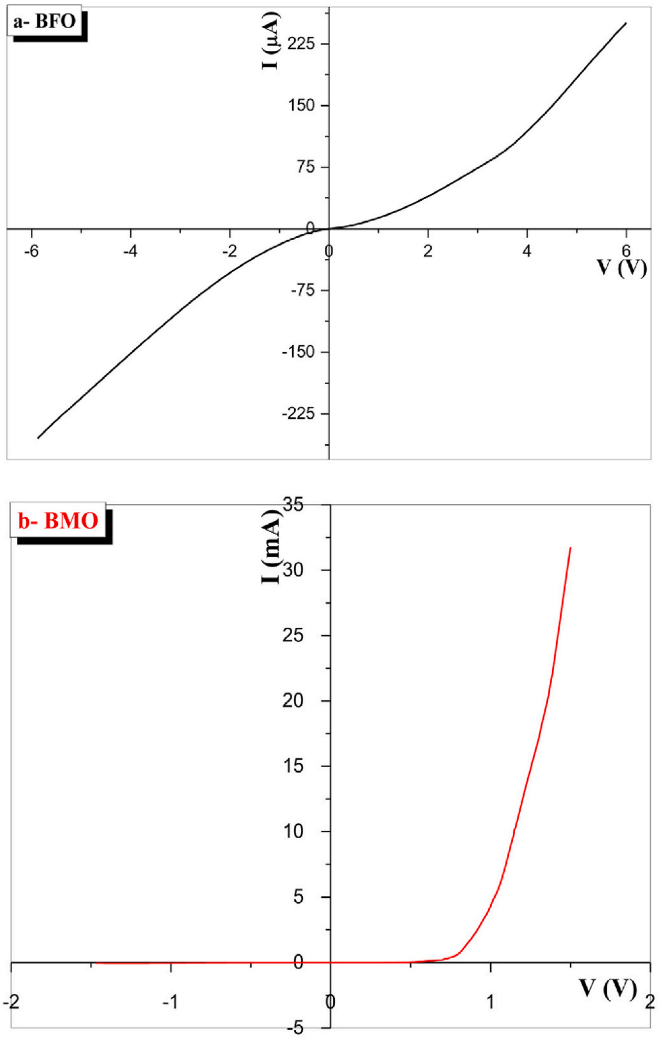

Fig. 9. I(V) characterization of the: (a) BFO/FTO and (b) BMO/NiO/FTO heterojunction.

$$I(V) = I_s\left(\exp\left(\frac{qV}{kTn}\right) - 1\right) \tag{4}$$

where k is Boltzmann constant, T the absolute temperature, q the elementary electronic charge, n the ideality factor and I_s the saturation current.

The ideality factor is extracted from the slope of the linear region in the forward-biased I-V curve and is calculated using the following expression [6]:

$$n = \frac{q}{kT}\left(\frac{dV}{d(\ln I)}\right) \tag{5}$$

The value of the effective barrier height (ϕ_b) was obtained using the following equation [6]:

$$\phi_b = \frac{k_B T}{q} Ln\left(\frac{AA^* T^2}{I_s}\right) \tag{6}$$

where A is the device area, A* is the Richardson constant.

Both curves exhibit a clear rectifying behavior, confirming the successful formation of p–n junctions in each structure. However, a distinct contrast in electrical performance is observed between the two devices, particularly in terms of series resistance R_s. The BFO/FTO structure demonstrates a significantly higher series resistance, which adversely affects charge transport and device performance. This elevated R_s in the BFO thin film can be explained by several contributing factors: (i) First, a poor energy band alignment between BFO and the FTO substrate is one of the main factors responsible for the high series resistance observed in the BFO/FTO structure. This imperfect alignment hinders efficient charge carrier transport, promotes charge accumulation at the interface, and results in a relatively high contact barrier estimated at approximately 0.70 eV. Furthermore, the presence of oxygen vacancies in BFO thin films, as reported in studies [54,55], exacerbates this issue. Indeed, the migration and accumulation of these vacancies at the interface induce band bending, which leads to a further increase in the barrier height (Table 4). This phenomenon is similar to that observed in $BFO/La_{0.7}Sr_{0.3}MnO_3$ heterojunctions, as described in the literature [55]. (ii) Second, BFO exhibits lower electrical conductivity compared to BMO, as shown in Table 3. This is mainly due to its lower charge carrier density. (iii) Finally, the low electrical conductivity observed in $BiFeO_3$ thin films, despite their good crystallinity and low defect density (see Table 2), indicates a significant hindrance to charge transport. This limitation is likely associated with an internal electric field opposing the applied bias, which originates from a misaligned spontaneous polarization within the $BiFeO_3$/FTO structure. Furthermore, the BMO/NiO/FTO heterostructure exhibits a significantly higher saturation current and a markedly lower series resistance, indicating improved charge transport properties. This enhanced performance can be attributed to the synergistic effects of the BMO and NiO layers. BMO, as an n-type semiconductor with relatively high electron mobility, facilitates efficient charge carrier generation and transport. Additionally, its low surface roughness and moderately hydrophobic nature benefit from improved adhesion provided by the NiO interlayer, which enhances surface energy balance and interfacial compatibility. The NiO layer also plays a crucial role in reducing the contact barrier (∼0.52 eV), optimizing band alignment, and acting as a selective transport layer that limits carrier recombination. Thus, the combination of favorable surface morphology, moderate hydrophobicity, and optimized interfacial properties contributes to the improved electrical performance of the device.

The ideality factor is determined according to the Schottky diode equation and generally varies from 1 to 2, depending on the manufacturing process and semiconductor material, it is used to determine which transport mechanism through the heterojunction is dominant. In the case where n is 1, diffusion is the dominant mechanism, whereas if $n > 2$, recombination and generation in the depletion layer is the dominant mechanism [37]. The ideality factor obtained for the BMO/NiO/FTO structure (see Table 4) is slightly greater than 1, yet remains close to unity, suggesting that charge transport is predominantly governed by diffusion mechanisms. This near-ideal diode behavior can be attributed to the relatively low bandgap of $BiMnO_3$, which facilitates carrier excitation, and the absence of strong internal polarization fields, commonly observed in ferroelectric materials. Together, these factors promote efficient charge injection and transport across the heterojunction interface. However, for the BFO/FTO structure, the ideality factor obtained is greater than 2, suggesting the presence of interface states and defects in the space charge region. These defects act as traps for charge carriers, thus affecting the electrical performance of the structure [56]. Moreover, the large value of the ideality factor for the BFO/FTO heterojunction can be attributed to various factors related to the structure and electronic properties of the junction. First, the recombination of electrons and holes in the depletion region can lead to a deviation of the current from the ideal curve [57]. Then, the trap-assisted tunneling phenomenon due to defects or impurities in the crystal structure can facilitate the charge transport [58]. In addition, carrier leakage [59], non-homogeneities in the junction barrier heights [60] and the presence of a strong internal electric field generated by the misaligned spontaneous polarization inherent to the ferroelectric $BiFeO_3$, which opposes the externally applied bias and hinders carrier mobility.

Table 4

Electrical setting of the BFO/FTO and BMO/NiO/FTO heterojunctions.

Structure	R_s, (Ω)	n, (cm^{-3})	Is, (A)	$φ_b$, (eV)
BFO/FTO	3.81×10^3	2.67	1.65×10^{-6}	0.70
BMO/NiO/FTO	13.32	1.83	0.6×10^{-3}	0.52

4. Conclusions

A spray pyrolysis method was successfully employed to prepare BFO and BMO thin films on conventional glass substrates. XRD analysis confirmed the polycrystalline nature of the samples, revealing a rhombohedral perovskite structure for BMO and a monoclinic perovskite structure for BFO, both characteristic of their ferroelectric behavior. Notably, the BMO film stood out by exhibiting a significantly high strain value, measured at 4.78×10^{-3}, which is markedly higher than that observed in the BFO film. This substantial strain is closely associated with a notable improvement in the optoelectronic properties of the BMO film. Raman spectroscopy analyses not only confirmed the presence of distinct crystal structures for each film but also highlighted a characteristic lattice distortion in the BMO film. The EDS spectra confirmed the presence of all the expected constituent elements in both BFO and BMO thin films. Atomic force microscopy (AFM) analysis revealed a substantially lower surface roughness for BMO (29.38 nm) compared to BFO (512.1 nm). Contact angle (CA) measurements showed values exceeding 90° for both films, indicating their hydrophobic nature an advantageous feature for thin-film solar cell applications. These findings are consistent with the AFM results. Optical characterization demonstrated that the BMO film possesses a reduced optical bandgap of approximately 1.2 eV and exhibits strong visible light absorption, evidenced by a low transmittance of around 2 %. Electrical measurements indicated improved properties for BMO, with a low resistivity of $1.90 \times 10^{+1}$ Ω cm and increased free carrier concentration. Furthermore, the hydrophobic surface nature, with a CA $\leq 93°$, likely contributes to the enhanced free carrier density, leading to superior electrical performance alongside the favorable optical properties of reduced transmittance and bandgap. Additionally, current-voltage (I-V) characterization of the fabricated solar cells (BFO/FTO and BMO/NiO/FTO) revealed superior performance for the BMO-based device, characterized by a low ideality factor of 1.83, a reduced series resistance of 13.32 Ω, and a low effective barrier height of 0.52 eV. The optimal bandgap value combined with the reduced ideality factor and series resistance in the hydrophobic BMO film prepared by spray pyrolysis represents a promising approach to enhance ferroelectric photovoltaic effects and other optoelectronic functionalities.

CRediT authorship contribution statement

Rayene Merah: Writing – review & editing, Writing – original draft, Visualization, Validation, Software, Resources, Methodology, Investigation. **Warda Darenfad:** Visualization, Supervision, Resources, Project administration, Funding acquisition, Formal analysis, Data curation, Conceptualization. **Kamel Mirouh:** Visualization, Validation, Software, Resources, Investigation, Funding acquisition. **Noubeil Guermat:** Validation, Software, Resources, Project administration, Funding acquisition, Data curation, Conceptualization. **Nadir Bouarissa:** Visualization, Validation, Resources, Investigation, Funding acquisition, Formal analysis.

Funding

This work is supported by the Research Project University-Formation

(PRFU) of Algerian ministry of high education and scientific research (No. A10N01UN280120220009). The project, titled 'Study, elaboration and characterization of the effect of doping and co-doping on the properties of oxides of transition metals for optoelectronic applications'.

Declaration of competing interest

The authors declare that they have no known competing financial interests or personal relationships that could have appeared to influence the work reported in this paper.

Data availability

No data was used for the research described in the article.

References

[1] A. Romeo, E. Artegiani, D. Menossi, Low substrate temperature CdTe solar cells: a review, Sol. Energy 175 (2018) 9–15, https://doi.org/10.1016/j.solener.2018.02.038.

[2] L.L. Yan, C. Han, B. Shi, Y. Zhao, X.D. Zhang, A review on the crystalline silicon bottom cell for monolithic perovskite/silicon tandem solar cells, Mater. Today Nano 7 (2019) 100045, https://doi.org/10.1016/j.mtnano.2019.100045.

[3] A. Gamoura, F.Z. Satour, A. Zegadi, A. Zouaoui, N. Bourouba, A comparative study on the effects induced following xenon ion implantation at high energies on the electrical, morphological and optical properties of $CuInSe_2$ monocrystalline, Opt. Mater. 149 (2024) 115061, https://doi.org/10.1016/j.optmat.2024.115061.

[4] T.A. Hameed, I.M. El Radaf, H.E. Elsayed Ali, Characterization of $CuInGeSe_4$ thin films and Al/n–Si/p–$CuInGeSe_4$/Au heterojunction device, J. Mater. Sci. Mater. Electron. 29 (2018) 12584–12594, https://doi.org/10.1007/s10854-018-9375-7.

[5] I.M. El Radaf, Dispersion parameters, linear and nonlinear optical analysis of the $SnSb_2S_4$ thin films, Appl. Phys. A 126 (357) (2020) 1–10, https://doi.org/10.1007/s00339-020-03543-0.

[6] M. Nasr, I.M. El Radaf, A.M. Mansour, Current transport and capacitance–voltage characteristics of an n-PbTe/p-GaP heterojunction prepared using the electron beam deposition technique, J. Phys. Chem. Solid. 115 (2018) 283–288, https://doi.org/10.1016/j.jpcs.2017.12.029.

[7] L. Xiang, F. Gao, Y. Cao, D. Li, Q. Liu, H. Liu, S. Li, Progress on the stability and encapsulation techniques of perovskite solar cells, Org. Electron. 106 (2022) 106515, https://doi.org/10.1016/j.orgel.2022.106515.

[8] X. Deng, Z. Zeng, R. Gao, Z. Wang, G. Chen, W. Cai, C. Fu, Study of structural, optical and enhanced multiferroic properties of Ni doped BFO thin films synthesized by sol-gel method, J. Alloys Compd. 831 (2020) 154857, https://doi.org/10.1016/j.jallcom.2020.154857.

[9] H. Matsuo, T. Sato, Y. Noguchi, Bulk photovoltaic effect in Cu-doped $LiNbO_3$ single crystals with controlled oxidation state, Jpn. J. Appl. Phys. 63 (2024), https://doi.org/10.35848/1347-4065/ad60cf, 07SP08.

[10] X. Luo, Y. Li, K. Liu, J. Zhang, Electron transport enhancement of perovskite solar cell due to spontaneous polarization of Li^+-doped $BaTiO_3$, Solid State Sci. 108 (2020) 106387, https://doi.org/10.1016/j.solidstatesciences.2020.106387.

[11] T.G. Lee, H.J. Lee, S.W. Kim, D.H. Kim, S.H. Han, H.W. Kang, S. Nahm, Piezoelectric properties of $Pb(Zr,Ti)O_3$-$Pb(Ni,Nb)O_3$ ceramics and their application in energy harvesters, J. Eur. Ceram. Soc. 37 (2017) 3935–3942, https://doi.org/10.1016/j.jeurceramsoc.2017.05.029.

[12] P. Prajapati, A.K. Singh, Development and characterization of (1-x) $BiYO_{3\text{-}x}BiMnO_3$ ceramics for Ferro-photovoltaic applications, Ceram. Int. 48 (2022) 25128–25139, https://doi.org/10.1016/j.ceramint.2022.05.173.

[13] M. Dewan, T. Majumder, S.B. Majumder, Electrophoretically deposited bismuth iron oxide as dual role anode material for both lithium and sodium-ion batteries, Mater. Today Commun. 27 (2021) 102358, https://doi.org/10.1016/j.mtcomm.2021.102358.

[14] L. Wu, J. Wang, G. Lan, W. Li, P. Meng, S. Jia, $BaTiO_3$-$BiMnO_3$ NTC thermistors for high-temperature batteries, J. Alloys Compd. 1011 (2025) 178396, https://doi.org/10.1016/j.jallcom.2024.178396.

[15] X. Li, F. Jia, J. Chen, D. Jin, W. Ren, J. Cheng, Enhanced photocatalytic activity of tourmaline modified $BiFeO_3$ nanoparticles by efficient charge transfer, Ceram. Int. 49 (2023) 34147–34154, https://doi.org/10.1016/j.ceramint.2023.08.121.

[16] Y. Qin, H. Luo, X. Yu, X. Song, W. Gao, H. Lai, J. Zhang, S. Zhu, M. Su, Photocatalytic degradation of tetracycline by a Fe-doped $BiMnO_3$ catalyst with honeycomb-like microstructure, Colloids Surf. A Physicochem. Eng. Asp. 673 (2023) 131784, https://doi.org/10.1016/j.colsurfa.2023.131784.

[17] T. Tong, J. Chen, D. Jin, J. Cheng, Preparation and gas sensing characteristics of $BiFeO_3$ crystallites, Mater. Lett. 197 (2017) 160–162, https://doi.org/10.1016/j.matlet.2017.03.091.

[18] B. Revathi, N. Krishna Chandar, Magnetic field sensing characteristics of rGO/$BiMnO_3$ nanocomposites loaded clad-modified optical fiber sensor, J. Sci. Adv. Mater. Devices 7 (2022) 100488, https://doi.org/10.1016/j.jsamd.2022.100488.

[19] S.S. Brahma, J. Nanda, N.K. Sahoo, B. Naik, A.A. Das, Phase transition, electronic transitions and visible light driven enhanced photocatalytic activity of Eu–Ni co-doped bismuth ferrite nanoparticles, J. Phys. Chem. Solid. 153 (2021) 110018, https://doi.org/10.1016/j.jpcs.2021.110018.

[20] N. Wang, X. Luo, L. Han, Z. Zhang, R. Zhang, H. Olin, Y. Yang, Structure, performance, and application of $BiFeO_3$ nanomaterials, Nano-Micro Lett. 12 (81) (2020) 1–23, https://doi.org/10.1007/s40820-020-00420-6.

[21] J. Li, J. He, S. Li, Y. Ren, K. Ding, S. Xing, Y. He, R. Gao, C. Fu, Microstructures and photovoltaic properties of TiO_2/$BiFeO_3$ core–shell nanowire arrays, J. Electron. Mater. 52 (2023) 3363–3373, https://doi.org/10.1007/s11664-023-10314-z.

[22] H.T. Sui, H.J. Sun, M. Li, X.F. Liu, Enhanced photovoltaic performance of sol–gel-derived FTO/TiO_2/$BiFeO_3$ heterostructure thin film obtained via modifying thickness of TiO_2 transport layer, J. Mater. Sci. Mater. Electron. 30 (2019) 933–938, https://doi.org/10.1007/s10854-018-0364-7.

[23] J. Chakrabartty, C. Harnagea, M. Celikin, F. Nechache, Improved photovoltaic performance from inorganic perovskite oxide thin films with mixed crystal phases, Nat. Photonics 12 (2018) 271–276, https://doi.org/10.1038/s41566-018-0137-0.

[24] T. Yang, J. Wei, Z. Sun, Y. Li, Z. Liu, Y. Xu, G. Chen, T. Wang, H. Sun, Z. Cheng, Design of oxygen vacancy in $BiFeO_3$-based films for higher photovoltaic performance, Appl. Surf. Sci. 575 (2022) 151713, https://doi.org/10.1016/j.apsusc.2021.151713.

[25] V. Singh, S. Sharma, R.K. Chourasia, A. Kumar, M. Kumar, Structural, dielectric, and leakage current analysis of 'La' doped $BiMnO_3$, Mater. Today Proc. (2023), https://doi.org/10.1016/j.matpr.2023.01.116.

[26] G.V. Umoh, J.T. Holguín-Momaca, R.P. Talamantes, G. Rojas-George, G. Herrera-Perez, R. Lopez Anton, Francisco Servando Aguirre-Tostado, O. Auciello, S.F. Olive Mendez, A. Hurtado-Macias, Influence of ex-situ thermal treatment on the chemical states, microstructure and ferroelectrics properties of polycrystalline $BiMnO_3$-δ thin films, Thin Solid Films 756 (2022) 139362, https://doi.org/10.1016/j.tsf.2022.139362.

[27] L. Meng, W. Xu, Q. Zhang, T. Yang, S. Shi, Study of nanostructural bismuth oxide films prepared by radio frequency reactive magnetron sputtering, Appl. Surf. Sci. 472 (2019) 165–171, https://doi.org/10.1016/j.apsusc.2018.02.0170.

[28] S. Ibrahim, P. Bonnet, M. Sarakha, C. Caperaa, G. Monier, A. Bousquet, Tailoring the structural and optical properties of bismuth oxide films deposited by reactive magnetron sputtering for photocatalytic application, Mater. Chem. Phys. 243 (2020) 122580, https://doi.org/10.1016/j.matchemphys.2019.122580.

[29] W. Darenfad, N. Guermat, N. Bouarissa, K. Mirouh, Investigation of structural, morphological and optoelectronic properties of (Ni, Co)-doped and (Ni/Co) co-doped SnO_2 (110) sprayed thin films, J. Mol. Struct. 1317 (2024) 138992, https://doi.org/10.1016/j.molstruc.2024.138992.

[30] W. Darenfad, N. Guermat, K. Mirouh, Thoughtful investigation of ZnO doped Mg and co-doped Mg/Mn, Mg/Mn/F thin films: a first study, J. Mol. Struct. 1286 (2023) 135574, https://doi.org/10.1016/j.molstruc.2023.135574.

[31] I. Bellili, M. Mahtali, W. Darenfad, N. Guermat, The figure of merit improvement of (Sn, Co)–ZnO sprayed thin films for optoelectronic applications, Opt. Mater. 154 (2024) 115785, https://doi.org/10.1016/j.optmat.2024.115785.

[32] O. Ceballos-Sanchez, A. Sanchez-Martinez, F.J. Flores-Ruiz, A.M. Huerta-Flores, Leticia M. Torres-Martínez, R. Ruelas, M. García-Guaderrama, Study of $BiFeO_3$ thin film obtained by a simple chemical method for the heterojunction-type solar cell design, J. Alloys Compd. 832 (2020) 154923, https://doi.org/10.1016/j.jallcom.2020.154923.

[33] Z.J. Hernandez Simon, J.A. Luna Lopez, J.A. David Hernandez De La Luz, G. O. Mendoza Conde, K. Monfil Leyva, O. Raymond Herrera, M. Moreno Moreno, H. P. Martinez Hernandez, E. Flores, Outstanding photoelectrical response in $BiFeO_3$ hollow microspheres deposited by ultrasonic spray pyrolysis technique, J. Alloys Compd. 955 (2023) 170215, https://doi.org/10.1016/j.jallcom.2023.170215.

[34] D. Nazipov, A. Nikiforov, L. Gonchar, Structure and lattice dynamics of Jahn-Teller crystal $BiMnO_3$: ab initio calculation, J. Phys.: Conf. Ser. 833 (2017) 012006, https://doi.org/10.1088/1742-6596/833/1/012006.

[35] D. Karoblis, A. Zarkov, K. Mazeika, D. Baltrunas, G. Niaura, A. Beganskiene, A. Kareiva, Sol-gel synthesis, structural, morphological and magnetic properties of $BaTiO_3$–$BiMnO_3$ solid solutions, Ceram. Int. 46 (2020) 16459–16464, https://doi.org/10.1016/j.ceramint.2020.03.209.

[36] N. Guermat, W. Darenfad, K. Mirouh, M. Kalfallah, M. Ghoumazi, Super-hydrophobic F-doped SnO_2 (FTO) nanoflowers deposited by spray pyrolysis process for solar cell applications, J. Nano- Electron. Phys. 15 (2022) 05013, https://doi.org/10.21272/jnep.14(5).05013.

[37] Z. Belamri, W. Darenfad, N. Guermat, Molarity dependence of solution on structural and hydrophobic properties of ZnO nanostructures, Eur. Phys. J. Appl. Phys. 99 (10) (2024), https://doi.org/10.1051/epjap/2024230146.

[38] Z. Belamri, W. Darenfad, N. Guermat, Impact of annealing temperature on surface reactivity of ZnO nanostructured thin films deposited on aluminum substrate, J. Nano- Electron. Phys. 15 (2023) 02026, https://doi.org/10.21272/jnep.15(2).02026.

[39] W. Darenfad, N. Guermat, K. Mirouh, Deposition time dependent physical properties of semiconductor CuO sprayed thin films as solar absorber, Eur. Phys. J. Appl. Phys. 99 (2024) 17, https://doi.org/10.1051/epjap/2024230200.

[40] Y. Nezzari, W. Darenfad, K. Mirouh, N. Guermat, N. Bouarissa, Structural, wettability, optical, and electrical modifications by varying precursor solutions of sprayed Co3O4 thin films for solar cell applications, Eur. Phys. J. B 98 (2025) 44, https://doi.org/10.1140/epjb/s10051-025-00889-3.

[41] I. Bellili, W. Darenfad, N. Guermat, N. Bouarissa, Optimizing the structural, optical, hydrophobic, and electrical properties of (Sn/Mg) co-doped ZnO thin films for application as solar cell electrodes, J. Mater. Sci. Mater. Electron. 36 (2025) 872, https://doi.org/10.1007/s10854-025-14918-5.

[42] Y. Nezzari, W. Darenfad, K. Mirouh, N. Guermat, N. Bouarissa, R. Merah, Hydrophobic nickel doped Co_3O_4 sprayed thin films as solar absorber, Opt. Quant. Electron. 56 (2024) 951, https://doi.org/10.1007/s11082-024-06930-6.

[43] N. Guermat, W. Darenfad, K. Mirouh, N. Bouarissa, M. Khalfallah, A. Herbadji, Effects of zinc doping on structural, morphological, optical and electrical properties of SnO_2 thin films, Eur. Phys. J. Appl. Phys. 97 (2022) 14, https://doi.org/10.1051/epjap/2022210218.

[44] W. Daranfed, N. Guermat, K. Mirouh, Experimental study in the effect of precursors in Co_3O_4 thin films used as solar absorbers, Ann. Chim. -Sci Mat. 44 (2020) 121–126, https://doi.org/10.18280/acsm.440207.

[45] L. Zhang, J. Chen, L. Fan, Z. Pan, J. Wang, K. Ibrahim, J. Tian, X. Xing, Enhanced switchable photovoltaic response and ferromagnetic of Co-doped $BiFeO_3$ based ferroelectric thin films, J. Alloys Compd. 742 (2018) 351–355, https://doi.org/10.1016/j.jallcom.2018.01.270.

[46] Y. Xu, C. Deng, X. Wang, Bandgap modulation and phase boundary region of multiferroic Gd, Co co-doped $BiFeO_3$ thin film, AIP Adv. 13 (2023) 115004, https://doi.org/10.1063/5.0176617.

[47] H.W. Shin, J.Y. Son, Enhanced multiferroic properties of tetragonally strained epitaxial $BiMnO_3$ thin films grown on single crystal Rh substrates, Solid State Sci. 91 (2019) 7–9, https://doi.org/10.1016/j.solidstatesciences.2019.03.003.

[48] J. Li, Z.X. Tang, X.G. Tang, Q.X. Liu, Y.P. Jiang, Anneal temperature dependence of resistive switching and photoelectric properties of bismuth ferrite thin film prepared via sol–gel method, Flat. Chem. 28 (2021) 100266, https://doi.org/10.1016/j.flatc.2021.100266.

[49] J. Chakrabartty, D. Barba, L. Jin, D. Benetti, F. Rosei, R. Nechache, Photoelectrochemical properties of $BiMnO_3$ thin films and nanostructures, J. Power Sources 365 (2017) 162–168, https://doi.org/10.1016/j.jpowsour.2017.08.064.

[50] M.M. Mohamed, S.M. Reda, Ahmed A. Amer, Enhanced performance of $BiFeO_3$@ nitrogen doped TiO_2 core-shell structured nanocomposites: synergistic effect towards solar cell amplification, Arab. J. Chem. 13 (2020) 2611–2619, https://doi.org/10.1016/j.arabjc.2018.06.013.

[51] A. Tuluk, H. Brouwer, S. Van der Zwaag, Controlling the oxygen defects concentration in a pure $BiFeO_3$ bulk, ceramic, Materials 15 (2022) 6509, https://doi.org/10.3390/ma1519650.

[52] H. Kuang, J. Wang, J. Li, F.X. Hu, J.R. Sun, B.G. Shen, Electric field control of the small-polaron hopping conduction in spatial confined $Pr_{0.7}(Ca_{0.6}Sr_{0.4})_{0.3}MnO_3$/PMN-PT heterostructure, AIP Adv. 7 (2017) 055814, https://doi.org/10.1063/1.4974887.

[53] S. Hanif, M. Hassan, S. Riaz, S. Atiq, S.S. Hussain, S. Naseem, G. Murtaza, Structural, magnetic, dielectric and bonding properties of BiMnO3 grown by co-precipitation technique, Results Phys. 7 (2017) 3190–3195, https://doi.org/10.1016/j.rinp.2017.08.061.

[54] J.H. Lee, J.H. Jeon, C. Yoon, S. Lee, Y.S. Kim, T.J. Oh, Y.H. Kim, J. Park, T.K. Song, B.H. Park, Intrinsic defect-mediated conduction and resistive switching in multiferroic $BiFeO_3$ thin films epitaxially grown on $SrRuO_3$ bottom electrodes, Appl. Phys. Lett. 108 (2016) 112902, https://doi.org/10.1063/1.4944554.

[55] Q. Hongyan, Ferroelectric resistance switching in epitaxial $BiFeO_3/La_{0.7}Sr_{0.3}MnO_3$ heterostructures, Materials 16 (2023) 7198, https://doi.org/10.3390/ma16227198.

[56] W. Darenfad, N. Guermat, N. Bouarissa, F.Z. Satour, A. Zegadi, K. Mirouh, Improvement in optoelectronics and photovoltaic properties of p-Co_3O_4/n-ZnO heterojunction : effect of deposition time of sprayed Co_3O_4 thin films, J. Mater. Sci. Mater. Electron. 35 (2024) 162, https://doi.org/10.1007/s10854-023-11909-2.

[57] K. Mensah-Darkwa, R.O. Ocaya, A.G. Al-Sehemi, D. Yeboah, A. Dere, A.A. Al-Ghamdi, R.K. Gupta, F. Yakuphanoğlu, Optoelectronic enhancement of ZnO/p-Si Schottky barrier photodiodes by (Sn,Ti) co-doping, Phys. B Condens. Matter 667 (2023) 415155, https://doi.org/10.1016/j.physb.2023.415155.

[58] Z. Boutebakh, D. Batibay, M.S. Aida, Y.S. Ocak, N. Attaf, Thermal sulfurization effect on sprayed CZTS thin filmsproperties and CZTS/CdS solar cells performances, Mater. Res. Express 5 (2018) 015511, https://doi.org/10.1088/2053-1591/aaa6e5.

[59] V. Janardhanam, J.H. Kim, I. Jyothi, M.S. Kang, S.K. Lee, C.J. Choi, Carrier transport across $PtSe_2$/n-type GaN heterojunction, Vacuum 218 (2023) 112597, https://doi.org/10.1016/j.vacuum.2023.112597.

[60] P. Das, B. Pal, M. Das, S. Sil, D. Das, A. Layek, P.P. Ray, Findings of inhomogeneity in barrier height of Schottky junction Al/rGO-SnO_2 having anomaly in theoretical and experimental value of Richardson constant: a Gaussian approach, Results Phys. 42 (2022) 105996, https://doi.org/10.1016/j.rinp.2022.105996.